High efficiency solar cells from extremely low minority carrier lifetime substrates using radial junction nanowire architecture

Vidur Raj[1,], Kaushal Vora[2], Lan Fu[1], Hark Hoe Tan[1,*] and Chennupati Jagadish[1]*

[1]Department of Electronic Materials Engineering, Research School of Physics and Engineering, The Australian National University, Canberra, ACT 2601, Australia

[2]Australian National Fabrication Facility, Research School of Physics and Engineering, The Australian National University, Canberra, ACT 2601, Australia

E-mail: vidur.raj@anu.edu.au; hoe.tan@anu.edu.au

KEYWORDS

Nanowire solar cell, Radial junction, III-V, Heterojunction, Selective contact

ABSTRACT.

Currently, a significant amount of photovoltaic device cost is related to its requirement of high-quality absorber materials, especially in the case of III-V solar cells. Therefore, a technology that can transform a low cost, low minority carrier lifetime material into an efficient solar cell can be beneficial for future applications. Here, we transform an inefficient p-type InP substrate with a

minority carrier lifetime less than 100 ps into an efficient solar cell by utilizing a radial p-n junction nanowire architecture. We fabricate a p-InP/n-ZnO/AZO radial heterojunction nanowire solar cell to achieve a photovoltaic conversion efficiency of 17.1%, the best reported value for radial junction nanowire solar cells. The quantum efficiency of ~ 95 % (between 550 – 750 nm) and short circuit current density of 31.3 mA/cm^2 are amongst the best for InP solar cells. Besides, we also perform an advanced loss analysis of proposed solar cell to assess different loss mechanisms in the solar cell.

INTRODUCTION

Currently, a significant portion of photovoltaics cost is related to absorber materials, especially in high efficiency devices where extremely high-quality absorber materials are required [1-4]. It has been predicted that the requirement of a high quality absorber can be significantly eased by using a radial junction nanowire architecture [5-7], where the axis of light absorption and charge separation is decoupled such that high absorption and efficient charge carrier collection can separately be optimized for optimum performance [6]. In addition, nanowire solar cells have other important advantages such as: (a) high absorption, (b) flexibility in device structural designs such as radial junction and nanowire tandems are possible, (c) low volume of material usage and hence low cost, and (d) innovative growth/fabrication processes such as aerotaxy and lift-off are being developed as new means to enable high quality flexible nanowire devices with very low cost [8-15]. However, due to the large surface-to-volume ratio nanowires tend to have significantly higher surface recombination as compared to thin films, which can significantly deteriorate the overall device performance [16-18]. Also, it is well-known that additional challenges and complications arise when

doping and surface passivation has to be implemented in a radial p-n junction nanowire grown using bottom up epitaxial growth techniques [6, 11, 19-20].

Most recently, carrier-selective contacts have been used to eliminate the requirement of doped homojunction in planar solar cells [21-23]. In fact, almost all high efficiency solar cells developed recently use carrier selective contacts (also known as "passivating contacts" or "heterocontacts") in one form or the other [6, 24-27]. In addition to providing carrier selectivity, these selective contacts may also provide sufficient surface passivation and low contact resistance, leading to higher efficiencies [28]. Previously, oxide-based charge carrier selective contacts have also been used in planar InP solar cells to achieve a large V_{oc} and high efficiency [25, 29-30]. However, so far there is no report on the use of an electron selective contact (ESC) for InP nanowire solar cells.

Here, we show that a substrate with an extremely low minority carrier lifetime can be transformed into a highly efficient nanowire solar cell by utilizing the concept of the radial junction with a carrier selective contact. To form a radial p-n junction, we etch a heavily doped p-type InP substrate which has an extremely low minority carrier lifetime (less than 100 ps) to form the nanowire core, which is then coated with an n-type Aluminum Zinc Oxide (AZO)/ Zinc Oxide (ZnO) shell. These radial junction nanowire devices exceed an efficiency of 17%. We show that AZO/ZnO shell over InP core significantly enhances the absorption, electron selectivity, passivation, and built-in electric field of the solar cell to achieve a J_{sc} of more than 30 mA/cm^2 for filling ratio as low as 0.11. Moreover, an advanced loss analysis of the p-InP/n-ZnO/AZO radial heterojunction nanowire solar cell shows that series resistance, non-perfect IQE and current loss at maximum power point are major loss mechanisms in current solar cell. Most importantly, our proposed electron selective layer (ESL)-based radial junction nanowire solar cell will be particularly useful in conditions where growth and doping of nanowires can be challenging.

Further, in near future, the heterojunction solar cell can be combined with techniques such as aerotaxy [31-32] and nanowire lift-off [15] to fabricate low cost, high efficiency, highly stable, flexible III-V solar cells.

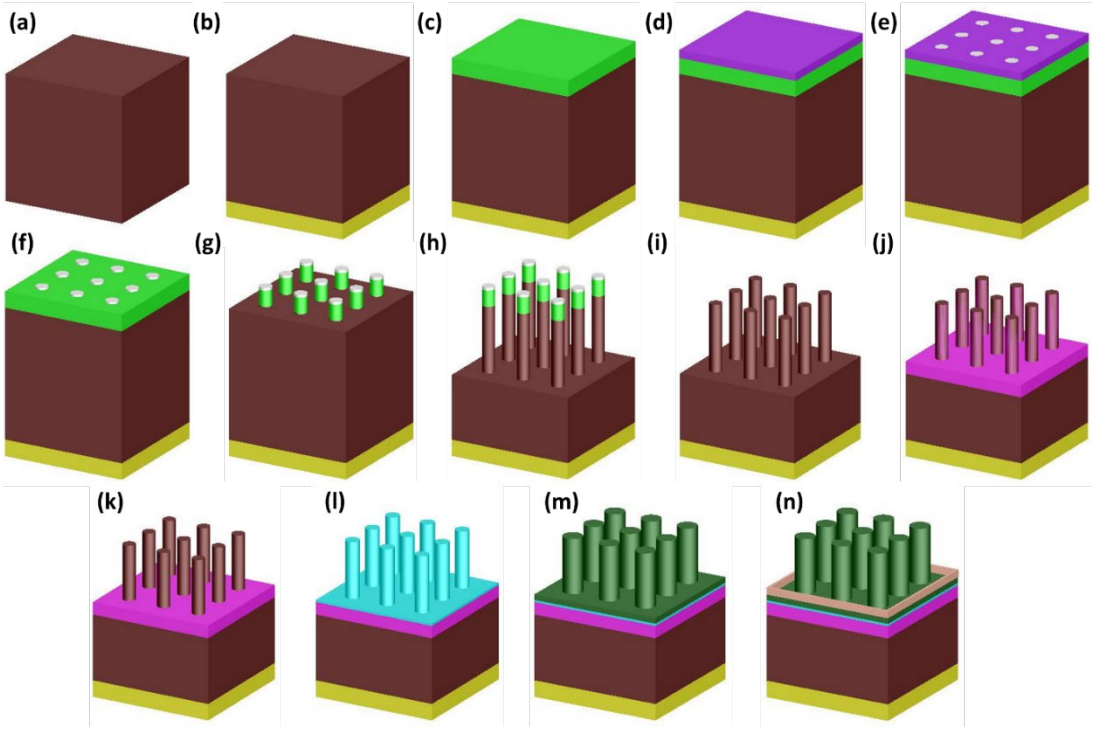

Figure 1. Fabrication sequence of the radial junction solar cell: (a) Cleaning of p-type InP substrate in 10% HF solution, (b) back contact deposition and annealing, (c) 600 nm-thick SiO_x deposition using PECVD, (d) e-beam resist coating, (e) e-beam exposure and development, (f) deposition of chromium and subsequent lift-off, (g) SiO_x etching, (h) InP etching, (i) SiO_x and chromium removal in 10% HF solution, (j) SU-8 spin coating with a thin layer of SU-8 coverage on side walls, (k) SU-8 coverage removal, exposure, baking and curing, (l) conformal 10 nm ZnO deposition in ALD, (m) subsequent deposition of 90 nm AZO, and (n) deposition of top-metal contact.

RESULTS and DISCUSSION

Figure 2(a) shows the 2-D schematic of the nanowire solar cell fabricated in this work. It consists of a p^+-InP core, a heavily doped n-type AZO/ZnO shell, and ~300 nm thick layer of SU-8 to isolate the radial heterojunction from the substrate. The ZnO layer acts as an electron selective layer as well as a passivation layer under optimized condition [6, 25], whereas AZO acts as a transparent conductor which facilitates the radial transport as well as the transport of electrons between metal contacts. In addition to carrier selectivity, passivation, and charge transport, an optimized thickness of ZnO/AZO also enhances the absorption in InP nanowires, as shown later in this section. Figure 2(b) shows a simulated band diagram of the AZO/ZnO/p-InP nanowire solar cell across the radial direction. ZnO for a type-II band alignment with InP with a large valence band offset, and a small conduction band offset, thereby allowing an easy flow of electron while impeding the flow of holes. Figure 2(c) shows the cross-sectional FESEM images of bare InP nanowires embedded in ~300 nm thick SU-8. Figures 2(d) shows the InP nanowires after conformal coating with a uniform 100 nm of ZnO/AZO (10 nm / 90 nm). Achieving a conformal and uniform thickness of AZO/ZnO layer along the length of the InP nanowire core is necessary to achieve high J_{sc} because optical absorption in InP nanowire is strongly dependent on the thickness of these oxide layers [6]. In inset of Figure 2(d), an example of nanowire solar cell with metal contact is shown. The total area of solar cell was defined as the area covered by the nanowire array. However, for calculation of active area efficiency, the area covered with metal was subtracted from the total area of the solar cell.

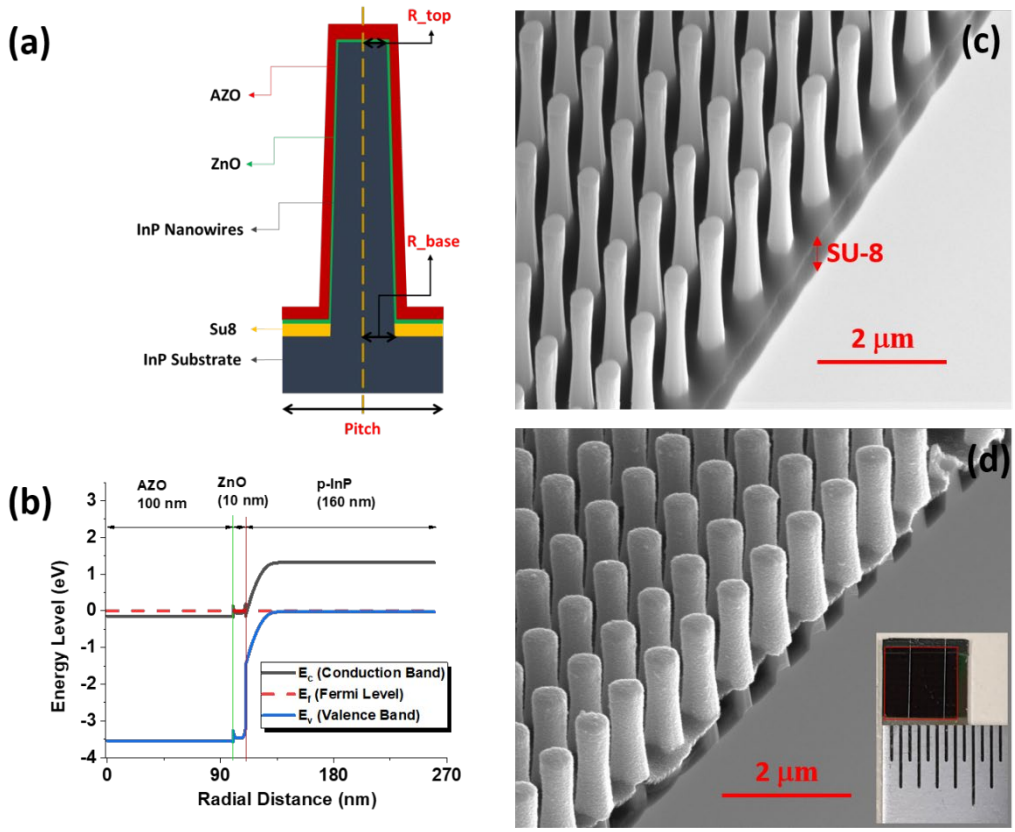

Figure 2. (a) 2-D schematic of the heterojunction solar cell. (b) Simulated Band diagram of AZO/ZnO/p-InP solar cell across radial direction. (c) shows the cross-sectional FESEM image of InP nanowires embedded in SU-8, (d) shows the FESEM image of the InP nanowires coated conformally and uniformly with 100 nm of ZnO/AZO (10 nm / 90 nm). **Inset:** A completed 4mm x 4mm nanowire solar cell (shown against a ruler –mm scale) with metal contact over it. The area of the solar cell corresponds to the area covered with nanowires (shown using red line boundary).

Low sheet resistance AZO is critical to achieving high factor as well as to ensure low contact resistance. Previously, AZO sheet resistance has been reported to be dependent on temperature

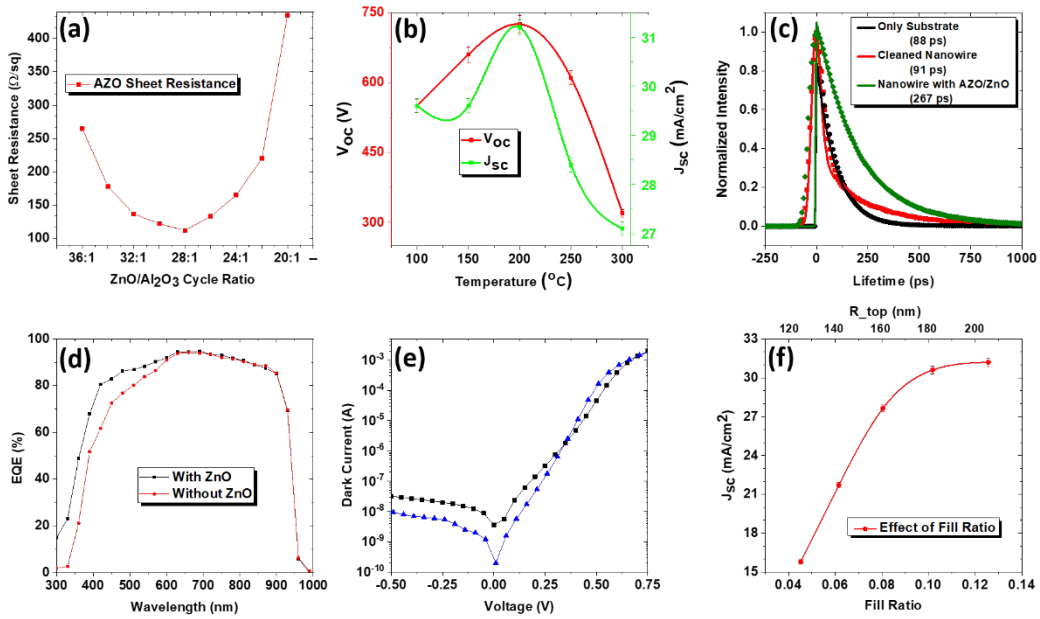

Figure 3. (a) Optimization of ZnO:Al_2O_3 cycle ratio to achieve lowest possible sheet resistance in AZO. (b) Effect of ZnO deposition temperature on V_{oc} and J_{sc} of the solar cell. (c) Carrier lifetime measurements on bare p+-InP substrate, InP nanowire, and nanowire coated with ZnO. Solid lines are single exponential fitting to the experimental data points. Note that for both nanowire samples, a chemical treatment was used to remove the surface damage induced by the plasma etching process. (d) Comparative EQE measurement on nanowire array solar cell with and without ZnO. (e) Dark current vs. voltage curve for the nanowire heterojunction solar cell, with and without ZnO. (f) Effect of geometric filling ratio on Jsc of the heterojunction solar cell. On top of x-axis, R_top denotes the top radius of nanocone.

and ZnO/Al_2O_3 cycle ratio [33-34]. To optimize the AZO sheet resistance, we set the optimum temperature for AZO deposition at 200 ºC based on ZnO optimization (discussed later) and then change the ZnO/Al_2O_3 cycle ratio to achieve minimum possible sheet resistance. Figure 3(a) shows the effect of ZnO/Al_2O_3 cycle ratio on the sheet resistance of AZO. Minimum sheet resistance for

AZO deposited using diffusion enhanced ALD (discussed in experimental section) was obtained for ZnO/Al_2O_3 cycle ratio of 28:1. Initially, increasing the ZnO/Al_2O_3 cycle ratio decreases the sheet resistance of AZO, however, after achieving the minimum sheet resistance of 112 Ω sq^{-1} for ZnO/Al_2O_3 cycle ratio of 28:1, the sheet resistance starts increasing again with increasing ZnO/Al_2O_3 cycle ratio. Similar results have been reported by several of the other authors [33-37]. An increase in AZO conductivity with increased Al_2O_3 is because of additional electrons that are introduced in AZO lattice by the substitution of Al^{3+} to the Zn^{2+} sites; whereas, after reaching the minimum sheet resistance at an optimum $ZnO:Al_2O_3$ ratio, the sheet resistance of AZO starts increasing because of a phenomenon called dopant clustering [33-34].

In current device, we use ZnO as an ESL because it forms a type-II heterojunction with p-type InP with a small conduction band offset and a large valence band offset, which allows the flow of electrons but impedes the flow of holes (see band diagram in Figure 2(b)) [6, 25]. Another critical parameter for ESL is its electrons conductivity in comparison to holes conductivity [6, 25, 28]. Higher electron conductivity leads to higher electron selectivity. The electron conductivity of ZnO is directly proportional to its n-type doping concentration, and therefore it is crucial to optimize the deposition conditions to achieve high doping. Under a given ALD condition (such as pressure, precursor flow rate, purge time, etc.), the doping level of ZnO is mainly dependent on the temperature [38-40]. Therefore, we deposit ZnO at different temperatures and study its effect on solar cell performance parameters of the heterojunction solar cells. As expected, both the V_{oc} and the J_{sc} (see Figure 3(b)) increases with increased ZnO deposition temperature until 200 ^oC, after which any further increase in temperature leads to a deterioration of V_{oc} and J_{sc}. An initial increase in V_{oc} and J_{sc} with increasing temperature is due to the increased n-type doping in ZnO from $7x10^{16}$ cm^{-3} at 50 ^oC to $4x10^{19}$ cm^{-3} at 200 ^oC, as confirmed by Hall effect measurements. Although the doping

level of ZnO increases to $6x10^{19}$ cm^{-3} at 250 ºC and $3x10^{20}$ cm^{-3} at 300 ºC, the SU-8 layer starts to decompose after 250 ºC resulting in deterioration of ZnO/InP interface quality which leads to higher interface recombination. Consequently, the V_{oc} decreases significantly from 725 mV at 200 ºC to 310 mV at 300 ºC.

Furthermore, we recently reported that the ZnO can chemically passivate the InP through the formation of $In(PO)_x$ at the ZnO/InP interface [25]. Therefore, to study on the passivation effect of ZnO deposition on InP nanowire surface, we perform lifetime, EQE, and dark current measurements on InP nanowire array solar cells with and without ZnO. Comparative lifetime measurements of the substrate and nanowire array with and without oxide are shown Figure 3(c). The lifetime of substrate is used as a reference to monitor the quality of the etched nanowires. It is well-known that the lifetime of the nanowire fabricated by top-down etching is significantly lower as compared to the substrate due to plasma-induced damage at the surface region [41-42]. Therefore, for both the nanowire samples (with and without oxide) shown in Figure 3 (c), the surface damage was removed using the method described earlier in the experimental section. As expected, nanowires coated with ZnO show an improved lifetime (267 ps) over bare InP nanowires (91 ps), which can be ascribed to the passivation of InP due to the formation of $In(PO)_x$ at the ZnO/InP interface [25]. We also performed comparative EQE and dark current measurements with and without ZnO to assess the effect of ZnO passivation on current solar cell. Figure 3(d) shows the EQE curve measured for AZO/p-InP and AZO/ZnO/p-InP solar cells. It is quite evident that with optimized ZnO layer, the quantum efficiency improved by almost 10-20% within 300-600 nm wavelength regime. The improvement in quantum efficiency in shorter wavelength regime is a result of improved surface passivation of the nanowire array after ZnO deposition. Furthermore, Figure 3(e) shows the comparative dark current vs. voltage curve of the heterojunction solar cell, with and

without ZnO deposition. Similar to EQE and minority carrier lifetime measurements, application of ZnO on nanowire significantly improves the behavior of nanowire solar cell in the dark. It is apparent that both the reverse leakage and the dark saturation current are reduced by almost an order of magnitude.

Additional advantages of the proposed core-shell structure are the possibility of achieving high radial built-in electric field along with an improved absorption [6], under optimized conditions. Because, ZnO and AZO can be heavily n-type doped to the order of 10^{19} cm^{-3}, a radial built-in electric field higher than 10^6 V/cm (see Figure S2 of the supplementary information) can easily be achieved with a p-type core doping of $3x10^{18}$ cm^{-3}. Such high built-in electric field is critical to achieving efficient charge carrier separation and collection when the bulk lifetime (or diffusion length) of the material is extremely low. Because, in case where minority carrier lifetime is low, charge carriers need to be separated through drift instead of diffusion otherwise they will recombine (due to low diffusion length) before they can be collected. In addition to a high built-in electric field, a shell of AZO/ZnO can significantly improve the absorption in InP nanowire because of reduced screening of incident electric field and an optical antenna effect [6, 43-45]. In other words, a dielectric shell enhances the coupling of light in InP nanowire and causes excitation of optical resonant modes, which in turn leads to enhanced absorption. As a combined result of the high radial built-in electric field, enhanced absorption, electron selectivity, and passivation, the proposed core-shell solar cell can achieve very high J_{sc} even for very low geometric filling ratio, as shown in Figure 3(f). The geometric filling ratio (for definition see supplementary information Figure S4) for a tapered nanowire (or nanocone) can be written as:

$$Filling\ Ratio\ (FR) = \frac{1}{3}\,\pi\,\frac{R_{top}^2 + R_{top}\,.\,R_{base} + R_{base}^2}{Pitch^2} \qquad (1)$$

where, *Pitch*, $R_{top,}$ and R_{Base} are the pitch, the radius of top and base of the bare nanowire that is shown schematically in Figure 1(a). To study the effect of geometric filling ratio, we fix the pitch of nanowire and vary the radii to achieve a particular filling factor. Figure 3 (f) shows the effect of geometric filling ratio on the measured J_{sc} of the nanowire solar cell. In Figure 3(f), top of x-axis denotes, R_top, the top radius of nanocone, and the length and pitch of nanowire array were fixed at 2 μm and 1 μm, respectively. An initial increase in J_{sc} with the increasing geometric filling ratio is due to an increase in the volume of the absorber, leading to increased absorption. At the same time, J_{sc} starts saturating after the FR of 0.11, because there is no significant enhancement in absorption after FR reaches 0.11. In the presence of an optimized oxide shell thickness and deposition conditions, a maximum J_{sc} of more than 31.2 mA/cm^2 can be achieved for a filling ratio as low as 0.13, which agrees well with recently reported simulation results [6]. Previously, several theoretical as well as experimental reports on InP nanowire solar cells show that to achieve a J_{sc} higher than 30 mA/cm^2, InP filling ratio should be more than 0.17 [6, 46-47]. However, in presence of an AZO/ZnO shell, a J_{sc} of more than 30 mA/cm^2 can be achieved for filling ratio as low as 0.11. In other words, use of AZO/ZnO shell over InP nanowires can significantly improve the absorption and charge carrier separation to reduce the material consumption by almost 3 times, in comparison to bare InP nanowires. This result can mainly be of significance when nanowire is grown using bottom-up methods.

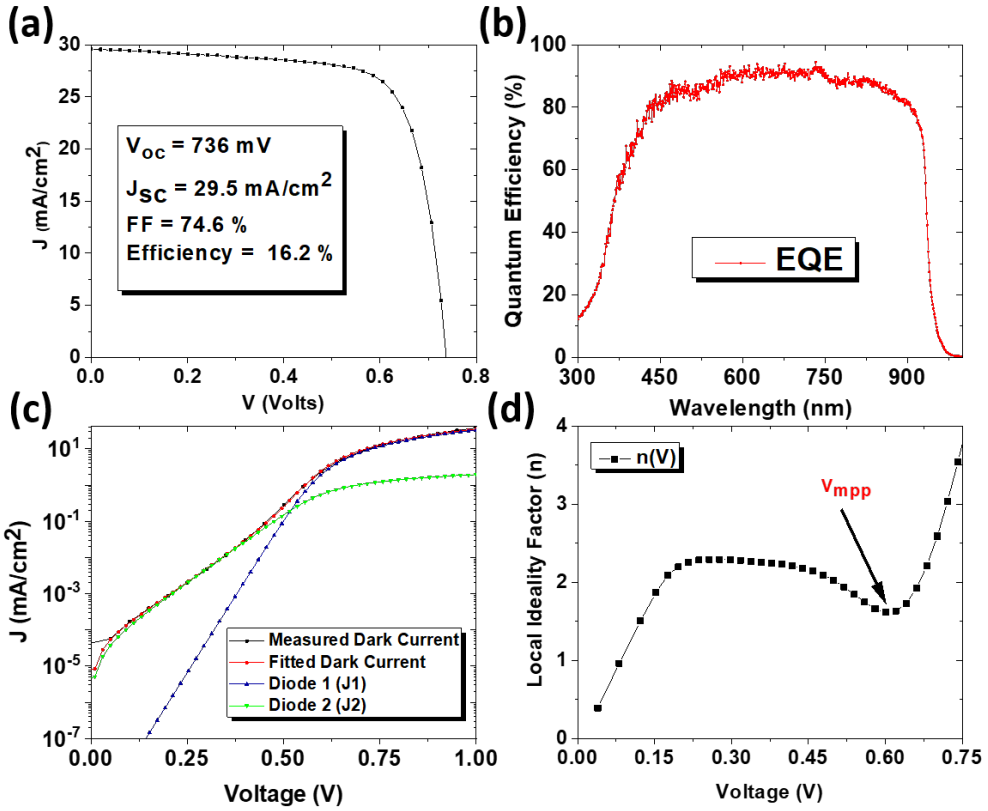

Figure 4. (a) I-V characteristics (1 sun@AM1.5 G), (b) EQE, (c) two-diode fitting and (d) local ideality factor vs voltage (n-V) curve of the radial junction nanowire solar cell. The V_{mpp} shows the maximum power point of the IV curve.

Figure 4(a) shows the I-V characteristics obtained from our best nanowire solar cell, exhibiting an efficiency of 16.2% with a V_{oc} of 736 mV, J_{sc} of 29.5 mA/cm^2 and a fill factor of 74.6%. For our best solar cell device, R_top and R_bottom of nanowire arrays were ~190 nm and ~230 nm, respectively, whereas, the pitch and length of nanowire array were fixed at 1µm and 2µm, respectively. The active area efficiency calculated after subtracting the ~6% metal coverage is 17.1% with a J_{sc} as high as 31.3 mA/cm^2, with the former representing the highest reported efficiency value for radial junction III-V nanowire solar cells and the latter representing the highest reported J_{sc} value for III-V nanowire solar cells, respectively. Moreover, not only is the proposed

device structure is efficient and simple, but it also reduces the device-related complexities of axial junction nanowire solar cells. For example, Wallentin et al. had shown that quantum efficiency, V_{oc}, and J_{sc} of an axial p-i-n junction solar cell depends heavily on the length of n-doped top segment; however, in current case, there is no p-i-n junction, and therefore there are no such limitations [48].

Furthermore, the high J_{sc} of our nanowire solar cell is also reflected in the measured EQE of the device as shown in Figure 4(b). In comparison to the best reported quantum efficiency for InP nanowire solar cell [48-49], the EQE of the present nanowire solar cells is ~ 10% higher for almost all measured wavelengths with the average quantum efficiency exceeding more than 90% in 550 – 750 nm wavelength, where most of the AM 1.5 solar spectrum lies. Moreover, by measuring the quantum efficiency in between the metal electrodes to eliminate the metal shadowing (see Figure 5(a)), a quantum efficiency exceeding 95% in the 550 – 750 nm regime is obtained. Such high quantum efficiency in our solar cells is direct evidence of highly efficient charge carrier generation, separation, and collection, even when the material lifetime is as low as 100 ps. Furthermore, the reproducibility of the device was assessed by fabricating five different devices in separate experiments. Tables S1 of the supplementary information shows the values of different solar cell parameters for different solar cells.

To better understand the main mechanisms that are limiting our solar cell performance, the device's dark I-V characteristics (Figure 4(c)) was fitted using the double-diode model [50] (for details see supplementary information) and extracted parameters are summarized in Table 1. The dark IV characteristic of a p-n junction can be fitted almost accurately using a double diode equation given as:

$$J = J_{01}\, exp\left[\frac{q(V - JR_s)}{kT}\right] + J_{02}\, exp\left[\frac{q(V - JR_s)}{n_2 kT}\right] + \frac{V - JR_s}{R_{Shunt}} \qquad (2)$$

where, J_{01} is the dark current contributions from ideal diode diffusion and $J_{02}$is the dark current due to recombination happening in the depletion region, and n_1 and n_2, are the ideality factors of respective diodes, whereas, R_s and R_{sh} are the series and shunt resistances, respectively. For our best solar cell, an exceptionally low J_{01} of 310 fA/cm^2 is obtained; however, J_{02} (56 nA/cm^2) is almost five orders of magnitude higher, indicating that the recombination current in this solar cell is mainly due to recombination in the depletion region. Such high depletion region recombination current is understandable considering that the device operates under a very built-in electric field, which effectively enhances the tunnelling recombination in the device by lowering the thermal barrier for recombination [51-53]. Note that field-enhanced tunnelling recombination is specific to the region of the device with high field strength, and therefore, it mainly affects the depletion region recombination [51-53]. The extracted series and shunt resistances are 7.6 Ω.cm^2 and 3x10^6 Ω.cm^2, respectively. The high series resistance accounts for the relatively low fill factor of 74.6%. Since the substrate and the nanowires are heavily doped and back contact is fully covered with a metal of extremely low contact resistance (10^{-5} Ω.cm^2), it is highly likely that most of the series resistance is due to AZO and the top metal contact. On the other hand, a very high shunt resistance of 3x10^6 Ω.cm^2 shows the excellent electrical isolation offered by SU-8. Figure 4(d) shows the calculated local ideality factor as a function of voltage. A local ideality factor higher than 2 is often considered to be originating from the isolated high recombination regions in the solar cell [54-56]. In our nanowire solar cell, the possible high recombination regions may include the broken nanowires, scratches and the edge of the nanowire array solar cells (damage due to mechanical cleaving) [54-56].

Table 1. Parameters extracted from the double diode fitting of the dark I-V curve under forward bias.

Symbol	Definition	Extracted Value
J_{01}	Saturation current density of diode 1	3.1 x 10^{-13} A/cm^2
J_{02}	Saturation current density of diode 2	5.6 x 10^{-8} A/cm^2
n_1	Ideality factor of diode 1.	1
n_2	Ideality factor of diode 2.	2.35
R_{sh}	Shunt Resistance	3 x 10^6 Ω.cm^2
R_s	Series Resistance	7.6 Ω.cm^2

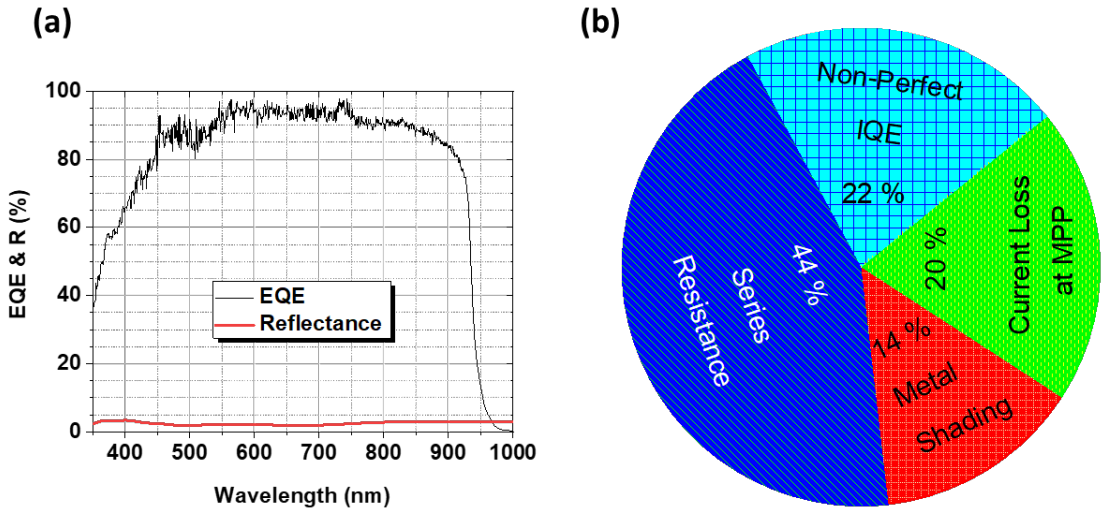

Figure 5. (a) EQE curve measured between metal electrodes for loss calculation due to non-perfect IQE. (b) A pie chart representation of the percentage contribution of different loss mechanisms to the total power loss of the solar cell at maximum power point.

To assess the losses and future potential of the ESL-based radial junction nanowire solar cell, we perform a detailed loss analysis based on the work of Armin et al.[57]. The loss analysis was performed on a solar cell reported in Figure 4. The loss mechanisms that we take into account are front metal shading, front surface reflectance, series resistance, shunt resistance, non-perfect IQE for wavelengths from 350 to 935 nm, and current loss at maximum power point. For calculation of loss due to non-perfect IQE, we measure the EQE and reflectance (R) between the metal electrodes to avoid any contribution from metal shading or reflectance as shown in Figure 5(a). A detailed mathematical formalism required to the calculation of different losses is given in the supplementary information. Table 2 summarizes the various losses of our solar cell at one-sun maximum power point (MPP). It is quite apparent that the power loss at MPP is mainly due to series resistance (3.27 mW/cm^2), followed by losses due to non-perfect IQE (1.59 mW/cm^2) and the current loss at the maximum power point (1.47 mW/cm^2). There is also a significant optical loss of around 1.028 mW/cm^2, mainly due to metal shading. A pie-chart representation of the percentage contribution of primary loss mechanisms to the total loss in the solar cell is given in Figure 5(b). This loss analysis suggests that the proposed radial junction nanowire solar cell has the potential to achieve higher efficiencies in near future.

Table 2. Contribution of different loss mechanisms at the maximum power point.

Type of Loss	Power loss (mW/sq.cm)
Metal Shading	1.00
Front surface reflectance (includes Front-Surface Escape)	0.028
Total optical losses (300 nm to 935 nm)	***1.028***
Series Resistance loss	3.27
Shunt Resistance loss	0.00

Total resistance losses	***3.27***
Non-perfect IQE	1.59
Forward-bias current loss at MPP	1.47
Recombination losses	***3.06***
Total Losses	***7.358***
Total efficiency potential of the solar cell	***23.56***

CONCLUSION

In this paper, we successfully demonstrate that an extremely low lifetime substrate can be converted into an efficient solar cell utilizing the radial junction nanowire architecture with carrier selective contacts. We fabricate a simple p-InP/n-ZnO/AZO heterojunction nanowire solar cell, which utilizes the efficient radial charge separation mechanism to achieve efficiency as high as 16.2 % even when the minority carrier lifetime of the InP substrate is less than 100 ps. For our best solar cell, we achieve an efficiency of 16.2 % (active area efficiency = 17.14 %) with a record J_{sc} of 29.54 mA/cm^2 (active area $J_{sc} \approx 31.3$ mA/cm^2). Such high efficiency and J_{sc} of core-shell heterojunction solar cell is a combined result of high absorption, high electron selectivity and passivation and a high radial built-in electric field exceeding 10^6 V/cm. An analysis of dark IV curve shows that recombination in the depletion region is a limiting factor for current solar cell. We also perform a detailed loss analysis of the heterojunction solar cell at the maximum power point to show that higher efficiency can be achieved for the proposed solar cell under optimum conditions. Finally, this work shows the huge potential of our radial heterojunction design to fabricate high efficiency solar cells using a substrate of very poor planar efficiency and low minority carrier lifetime, and can further be extended to other solar cell materials such as chalcogenides, silicon, and GaAs.

DEVICE FABRICATION TECHNIQUES

Figure 1 shows a 3-D schematic of the fabrication flow chart for the AZO/ZnO/p-InP nanowire array solar cell. The fabrication started with dipping of a p^+-InP substrate of thickness of 350 μm with a carrier concentration of ~$3x10^{18}$ cm^{-3} (from AXT Inc.), in 1% HF solution for native oxide removal (see Figure 1(a)). The wafer was then transferred into a ATC 1800 UHV sputter chamber to deposit the Zn:Au (10 nm:100 nm) back contact (see Figure 1(b)) which was then annealed at 400 °C in the presence of forming gas (5% H_2 and 95% N_2) to make an Ohmic contact. Subsequently, the wafer with back contact was transferred to a plasma-enhanced chemical vapor deposition system (Oxford Plasmalab 200) for 600 nm thick SiO_2 deposition (see Figure 1(c)). The deposition of SiO_2 was performed at 300 ºC under a pressure of 87 Pa and radio frequency power of 200 W using the $SiH_4/N_2O/N_2$ gases with a flow rate of 9/70/161 sccm, respectively. Next, the wafer with SiO_2 thin film was patterned using a RAITH 150 electron-beam lithography (EBL) system to open holes (see Figure 1(d) and 1(e)) of different diameters to achieve a specified geometric filling ratio, for a fixed pitch of 1000 nm over 4 mm x 4 mm area. The EBL patterned substrate was then transferred in the e-beam evaporator for deposition of 70 nm thick chromium layer. The substrate with chromium was then dipped for 1 hour in acetone at room temperature for lift-off. The lifted-off chromium (see Figure 1(f)) acted as a mask for SiO_2 etching, which acted as a mask for the inductively coupled plasma (ICP) etching of InP. An additional layer of SiO_2 helped reduce metal contamination as well as the removal of chromium after the etching. The ICP etching of SiO_2 (see Figure 1(g)) was performed in a commercial Samco RIE-400iP system at room temperature with a fixed pressure of 0.1 mTorr, CHF_3 flow rate of 20 sccm and an ICP/RF power of 400 W/80 W. The ICP (Samco RIE-400iP) etching of InP (see Figure 1(h)) was carried out at 180 °C electrode temperature by passing 1.5/25 sccm of $SiCl_4$/Ar gases at a chamber pressure of

0.1 Pa, with the RF/ICP powers of 50/200 W. Subsequently, SiO_x and chromium masks were removed by etching the SiO_x in 10% HF at room temperature for 5 minutes (see Figure 1(i)). However, due to surface damage caused by ICP etching, the lifetime of the nanowire was low compared to the substrate (see supplementary information Figure S1). To remove the surface damage, an additional processing step was used which involved barrel etching (PVA Tepla Gigabatch 310 M) of nanowire in oxygen plasma at 500 W for 30 s followed by HF (1% HF) cleaning and rinsing. After repeating this step three times the measured lifetime of nanowire was almost similar to that of the substrate. For all device fabrication and testing, we make use of these cleaned nanowire arrays.

The cleaned InP nanowire array was then spin coated with a ~350 nm thick SU-8 layer (see Figure 1(j)) to prevent the formation of a parasitic heterojunction between the p^+-substrate and the AZO/ZnO shell. Afterwards, the sample was put in a barrel etcher (PVA Tepla Gigabatch 310 M) for mild oxygen plasma treatment at 100 W for 2 min to remove any sidewall coverage of the SU-8 layer and clean the nanowires of any organic residue. The sample was then dipped in 1% HF for 1 minute to remove any possible oxidation due to barrel etching. The final thickness of SU-8 after oxygen plasma etching and HF cleaning was ~300 nm. To make SU-8 more robust and stable, it was cross-linked by exposure to conventional UV (350-400 nm) radiation, followed by a soft bake (@ 95 ºC for 10 minutes) and a hard bake (@200 ºC for 5 minutes) (see Figure 1(k)). SU-8 not only provides the electrical isolation from the substrate but also reinforces the mechanical strength of the nanowire array. Subsequently, atomic layer deposition (ALD) deposition of 10 nm of ZnO (see Figure 1(l)) and 100nm of AZO (see Figure 1(m)) was performed in a commercial ALD system from Picosun Inc. For all ALD depositions the chamber pressure was maintained at 9 Pa and the carrier gas (N_2) flow rate was fixed at 150 sccm. To achieve a highly conformal as well as

uniform AZO/ZnO layer, we make use of diffusion enhanced technique in ALD, utilizing a stop flow functionality to lengthen the time available for precursor diffusion and surface reaction on nanowire, leading to high conformality and uniformity in high-aspect ratio nanostructures. Finally, the front contact on the nanowire solar was made using a shadow mask with a finger width of ~60 μm.

DEVICE CHARACTERIZATION METHODS

The current-voltage (I-V) characteristic of the nanowire array solar cell was obtained using an Oriel solar simulator and IV test station, under the 1-sun @ Air mass 1.5 G (at 25 ºC) calibrated using a silicon reference cell. The total illuminated area of the solar cell considered during efficiency calculation is the area with the InP nanowire array (see inset of Figure 2(c)), i.e., 4mm x 4mm. The area with nanowires was predefined using highly accurate EBL patterning. To calculate active area efficiency, 6% of total metal shading was subtracted from the total area. Both dark and light measurements were performed in air at room temperature. Furthermore, we performed a separate light IV measurement by exposing the area without nanowires to make sure that there is no J_{sc} contribution from anywhere other than the area covered with nanowires. To assess the reproducibility of the proposed device, 5 different devices were tested. To perform the external quantum efficiency (EQE) measurement a NewSpec IQE-200 AC system was used and before each measurement, the EQE system was calibrated against a standard reference.

To perform the cross-sectional field emission scanning electron microscope (FESEM) of the nanowire array solar cell, the sample was cleaved along the (100) axis. The cross-sectional FESEM of the nanowire array solar cell was performed in FEI Verios system under the voltage of 5 kV and current of 0.16 nA. The sheet resistance of AZO was measured using a Jandel resistivity test equipment. For both ZnO and AZO, Hall effect measurements were performed at room

temperature in a Lakeshore Hall system at magnetic fields varying from -10 to + 10 kG, to assess the charge carrier concentration and conductivity. Time-resolved photoluminescence (TRPL) measurement was performed at room temperature using a Yb:YAG laser with a pulse duration of 300 fs, repetition rate of 20.8 MHz, frequency-doubled to a wavelength of 532 nm using a LBO crystal. The laser beam was directed on to the sample through a high numerical aperture (NA=0.9) objective with a magnification of 100x. At the laser repetition rate of 20 MHz, the average laser power of 1mW was equivalent to 48 pJ per pulse and the maximum power used for sample testing was 54.70 μW. Any further increase in laser power led to nanowire damage and quenched photoluminescence. A charge-coupled detector array was used to record the photoluminescence (PL) spectrum with a spectrometer and a Picoharp 300 time-correlated single photon counting system used to detect the PL decay. TRPL intensity decay at peak wavelength was fitted by a single-exponential decay to extract the minority carrier lifetime.

ASSOCIATED CONTENT

Supporting Information.

AUTHOR INFORMATION

Corresponding Author

*vidur.raj@anu.edu.au; *hoe.tan@anu.edu.au

Author Contributions

The manuscript was written through contributions of all authors. All authors have given approval to the final version of the manuscript.

Funding Sources

This work is supported by the Australian Research Council through the Discovery-Project grants.

ACKNOWLEDGMENT

This work is supported by the Australian Research Council through the Discovery-Project grants.

Access to the fabrication facilities is made possible through the support of the Australian

National Fabrication Facility, ACT Node.

REFERENCES

1. Ward, J. S.; Remo, T.; Horowitz, K.; Woodhouse, M.; Sopori, B.; VanSant, K.; Basore, P., Techno-economic analysis of three different substrate removal and reuse strategies for III-V solar cells. *Prog. Photovoltaics.* **2016,** *24* (9), 1284-1292.
2. Kelsey A. W. Horowitz, T. R., Brittany Smith, and Aaron Ptak *A Techno-Economic Analysis and Cost Reduction Roadmap for III-V Solar Cells*; National Renewable Energy Laboratory: Golden, Colarado, USA, 2018.
3. Greenaway, A. L.; Boucher, J. W.; Oener, S. Z.; Funch, C. J.; Boettcher, S. W., Low-Cost Approaches to III–V Semiconductor Growth for Photovoltaic Applications. *ACS Energy Lett.* **2017,** *2* (10), 2270-2282.
4. Goodrich, A.; Woodhouse, M. *A Manufacturing Cost Analysis Relevant to Single- and Dual-Junction Photovoltaic Cells Fabricated with III-Vs and III-Vs Grown on Czochralski Silicon*; National Renewable Energy Laboratory (NREL): Colarado, United States, 2013.
5. Kayes, B. M.; Atwater, H. A.; Lewis, N. S., Comparison of the device physics principles of planar and radial p-n junction nanorod solar cells. *J. Appl. Phys.* **2005,** *97* (11), 114302.
6. Vidur Raj, L. F., Hark Hoe Tan, Chennupati Jagadish, Design Principles for Fabrication of InP-Based Radial Junction Nanowire Solar Cells Using an Electron Selective Contact. *{IEEE} J. Photovolt.* **2019,** *9* (4), 980-991.
7. Shen, X.; Sun, B.; Liu, D.; Lee, S.-T., Hybrid Heterojunction Solar Cell Based on Organic–Inorganic Silicon Nanowire Array Architecture. *Journal of the American Chemical Society* **2011,** *133* (48), 19408-19415.
8. Garnett, E. C.; Brongersma, M. L.; Cui, Y.; McGehee, M. D., Nanowire Solar Cells. *Annu. Rev. Mater.Res.* **2011,** *41* (1), 269-295.
9. Li, Z.; Tan, H. H.; Jagadish, C.; Fu, L., III–V Semiconductor Single Nanowire Solar Cells: A Review. *Adv. Mater. Technol.* **2018,** *3* (9), 1800005.
10. Li, Z.; Wenas, Y. C.; Fu, L.; Mokkapati, S.; Tan, H. H.; Jagadish, C., Influence of Electrical Design on Core–Shell GaAs Nanowire Array Solar Cells. *{IEEE} J. Photovolt.* **2015,** *5* (3), 854-864.
11. Otnes, G.; Borgström, M. T., Towards high efficiency nanowire solar cells. *Nano Today* **2017,** *12*, 31-45.

12. Dhaka, V.; Haggren, T.; Jussila, H.; Jiang, H.; Kauppinen, E.; Huhtio, T.; Sopanen, M.; Lipsanen, H., High Quality GaAs Nanowires Grown on Glass Substrates. *Nano Lett.* **2012,** *12* (4), 1912-1918.
13. Meshram, N. P.; Kumbhar, A.; Dusane, R. O., Silicon nanowire growth on glass substrates using hot wire chemical vapor deposition. *Thin Solid Films* **2011,** *519* (14), 4609-4612.
14. Lee, C. H.; Kim, D. R.; Zheng, X., Fabricating nanowire devices on diverse substrates by simple transfer-printing methods. *Proc. Natl. Acad. Sci. (U. S. A.)* **2010,** *107* (22), 9950.
15. Dai, X.; Messanvi, A.; Zhang, H.; Durand, C.; Eymery, J.; Bougerol, C.; Julien, F. H.; Tchernycheva, M., Flexible Light-Emitting Diodes Based on Vertical Nitride Nanowires. *Nano Lett.* **2015,** *15* (10), 6958-6964.
16. Boland, J. L.; Casadei, A.; Tütüncüoglu, G.; Matteini, F.; Davies, C. L.; Jabeen, F.; Joyce, H. J.; Herz, L. M.; Fontcuberta i Morral, A.; Johnston, M. B., Increased Photoconductivity Lifetime in GaAs Nanowires by Controlled n-Type and p-Type Doping. *ACS Nano* **2016,** *10* (4), 4219-4227.
17. Gutsche, C.; Niepelt, R.; Gnauck, M.; Lysov, A.; Prost, W.; Ronning, C.; Tegude, F.-J., Direct Determination of Minority Carrier Diffusion Lengths at Axial GaAs Nanowire p–n Junctions. *Nano Lett.* **2012,** *12* (3), 1453-1458.
18. Triplett, M.; Yang, Y.; Léonard, F.; Talin, A. A.; Islam, M. S.; Yu, D., Long Minority Carrier Diffusion Lengths in Bridged Silicon Nanowires. *Nano Lett.* **2015,** *15* (1), 523-529.
19. Dayeh, S. A.; Chen, R.; Ro, Y. G.; Sim, J., Progress in doping semiconductor nanowires during growth. *Mat. Sci. Semicon. Proc.* **2017,** *62*, 135-155.
20. Haverkort, J. E. M.; Garnett, E. C.; Bakkers, E. P. A. M., Fundamentals of the nanowire solar cell: Optimization of the open circuit voltage. *Appl. Phys. Rev.* **2018,** *5* (3), 031106.
21. Bullock, J.; Hettick, M.; Geissbühler, J.; Ong, A. J.; Allen, T.; Sutter-Fella, Carolin M.; Chen, T.; Ota, H.; Schaler, E. W.; De Wolf, S.; Ballif, C.; Cuevas, A.; Javey, A., Efficient silicon solar cells with dopant-free asymmetric heterocontacts. *Nat. Energy* **2016,** *1*, 15031.
22. Bullock, J.; Wan, Y.; Xu, Z.; Essig, S.; Hettick, M.; Wang, H.; Ji, W.; Boccard, M.; Cuevas, A.; Ballif, C.; Javey, A., Stable Dopant-Free Asymmetric Heterocontact Silicon Solar Cells with Efficiencies above 20%. *ACS Energy Lett.* **2018,** *3* (3), 508-513.
23. Raj, V.; Lu, T.; Lockrey, M.; Liu, R.; Kremer, F.; Li, L.; Liu, Y.; Tan, H. H.; Jagadish, C., Introduction of TiO2 in CuI for Its Improved Performance as a p-Type Transparent Conductor. *ACS Appl. Mater. Interfaces* **2019,** *11* (27), 24254-24263.
24. Yoshikawa, K.; Kawasaki, H.; Yoshida, W.; Irie, T.; Konishi, K.; Nakano, K.; Uto, T.; Adachi, D.; Kanematsu, M.; Uzu, H.; Yamamoto, K., Silicon heterojunction solar cell with interdigitated back contacts for a photoconversion efficiency over 26%. *Nat. Energy* **2017,** *2*, 17032.
25. Raj, V. et al.; Indium phosphide based solar cell using ultra-thin ZnO as an electron selective layer. *J. Phys. D : Appl. Phys.* **2018,** *51* (39), 395301.
26. Masuko, K. et al.; Achievement of More Than 25% Conversion Efficiency With Crystalline Silicon Heterojunction Solar Cell. *{IEEE} J. Photovolt.* **2014,** *4* (6), 1433-1435.
27. Kato, T.; Handa, A.; Yagioka, T.; Matsuura, T.; Yamamoto, K.; Higashi, S.; Wu, J.; Tai, K. F.; Hiroi, H.; Yoshiyama, T.; Sakai, T.; Sugimoto, H., Enhanced Efficiency of Cd-Free Cu(In,Ga)(Se,S)2 Minimodule Via (Zn,Mg)O Second Buffer Layer and Alkali Metal Post-Treatment. *{IEEE} J. Photovolt.* **2017,** *7* (6), 1773-1780.

28. Cuevas, A.; Wan, Y.; Yan, D.; Samundsett, C.; Allen, T.; Zhang, X.; Cui, J.; Bullock, J., Carrier population control and surface passivation in solar cells. *Sol. Energ. Mat. Sol. C.* **2018,** *184*, 38-47.
29. Yin, X.; Battaglia, C.; Lin, Y.; Chen, K.; Hettick, M.; Zheng, M.; Chen, C.-Y.; Kiriya, D.; Javey, A., 19.2% Efficient InP Heterojunction Solar Cell with Electron-Selective TiO2 Contact. *ACS Photonics* **2014,** *1* (12), 1245-1250.
30. Oener, S. Z.; Cavalli, A.; Sun, H.; Haverkort, J. E. M.; Bakkers, E. P. A. M.; Garnett, E. C., Charge carrier-selective contacts for nanowire solar cells. *Nat. Commun.* **2018,** *9* (1), 3248.
31. Barrigón, E.; Hultin, O.; Lindgren, D.; Yadegari, F.; Magnusson, M. H.; Samuelson, L.; Johansson, L. I. M.; Björk, M. T., GaAs Nanowire pn-Junctions Produced by Low-Cost and High-Throughput Aerotaxy. *Nano Lett.* **2018,** *18* (2), 1088-1092.
32. Metaferia, W.; Sivakumar, S.; Persson, A. R.; Geijselaers, I.; Wallenberg, L. R.; Deppert, K.; Samuelson, L.; Magnusson, M. H., n-type doping and morphology of GaAs nanowires in Aerotaxy. *Nanotechnology* **2018,** *29* (28), 285601.
33. Lee, D.-J.; Kim, H.-M.; Kwon, J.-Y.; Choi, H.; Kim, S.-H.; Kim, K.-B., Structural and Electrical Properties of Atomic Layer Deposited Al-Doped ZnO Films. *Adv. Funct. Mater.* **2011,** *21* (3), 448-455.
34. Kan, Z.; Wang, Z.; Firdaus, Y.; Babics, M.; Alshareef, Husam N.; Beaujuge, P. M., Atomic-layer-deposited AZO outperforms ITO in high-efficiency polymer solar cells. *J. Mater. Chem. A* **2018,** *6* (22), 10176-10183.
35. Dasgupta, N. P.; Neubert, S.; Lee, W.; Trejo, O.; Lee, J.-R.; Prinz, F. B., Atomic Layer Deposition of Al-doped ZnO Films: Effect of Grain Orientation on Conductivity. *Chem. Mater.* **2010,** *22* (16), 4769-4775.
36. Luka, G.; Krajewski, T. A.; Witkowski, B. S.; Wisz, G.; Virt, I. S.; Guziewicz, E.; Godlewski, M., Aluminum-doped zinc oxide films grown by atomic layer deposition for transparent electrode applications. *J. Mater. Sci.: Mater. Electron.* **2011,** *22* (12), 1810-1815.
37. Dhakal, T.; Nandur, A.; Christian, R.; Vanhart, D.; Vasekar, P.; Westgate, C. R., Growth of AZO on flexible substrate using ALD system as a transparent conducting oxide for solar cells. *MRS Proc.* **2011,** *1327*, mrss11-1327-g03-24.
38. Gong, S. C.; Bang, S.; Jeon, H.; Park, H.-H.; Chang, Y. C.; Chang, H. J., Effects of atomic layer deposition temperatures on structural and electrical properties of ZnO films and its thin film transistors. *Met. Mater. Int.* **2010,** *16* (6), 953-958.
39. Macco, B.; Knoops, H. C. M.; Verheijen, M. A.; Beyer, W.; Creatore, M.; Kessels, W. M. M., Atomic layer deposition of high-mobility hydrogen-doped zinc oxide. *Sol. Energ. Mat. Sol. C.* **2017,** *173*, 111-119.
40. Kang, K.-M.; Park, H.-H., Effect of Atomic Layer Deposition Temperature on the Growth Orientation, Morphology, and Electrical, Optical, and Band-Structural Properties of ZnO and Fluorine-Doped ZnO Thin Films. *J. Phys. Chem. C* **2018,** *122* (1), 377-385.
41. Zin, N. S.; Blakers, A.; Weber, K., RIE-induced carrier lifetime degradation. *Prog. Photovoltaics.* **2010,** *18* (3), 214-220.
42. Asakawa, K.; Yoshikawa, T.; Kohmoto, S.; Nambu, Y.; Sugimoto, Y., Chlorine-Based Dry Etching of III/V Compound Semiconductors for Optoelectronic Application. *Jpn. J. Appl. Phys.* **1998,** *37* (Part 1, No. 2), 373-387.
43. Anttu, N.; Namazi, K. L.; Wu, P. M.; Yang, P.; Xu, H.; Xu, H. Q.; Håkanson, U., Drastically increased absorption in vertical semiconductor nanowire arrays: A non-absorbing dielectric shell makes the difference. *Nano Research* **2012,** *5* (12), 863-874.

44. Yu, Y.; Ferry, V. E.; Alivisatos, A. P.; Cao, L., Dielectric Core–Shell Optical Antennas for Strong Solar Absorption Enhancement. *Nano Lett.* **2012,** *12* (7), 3674-3681.
45. Zhong, Z.; Li, Z.; Gao, Q.; Li, Z.; Peng, K.; Li, L.; Mokkapati, S.; Vora, K.; Wu, J.; Zhang, G.; Wang, Z.; Fu, L.; Tan, H. H.; Jagadish, C., Efficiency enhancement of axial junction InP single nanowire solar cells by dielectric coating. *Nano Energy* **2016,** *28*, 106-114.
46. Anttu, N.; Xu, H. Q., Efficient light management in vertical nanowire arrays for photovoltaics. *Opt. Express* **2013,** *21* (S3), A558-A575.
47. Wu, D.; Tang, X.; Wang, K.; He, Z.; Li, X., An Efficient and Effective Design of InP Nanowires for Maximal Solar Energy Harvesting. *Nanoscale Res. Lett.* **2017,** *12* (1), 604.
48. Wallentin, J.; Anttu, N.; Asoli, D.; Huffman, M.; Åberg, I.; Magnusson, M. H.; Siefer, G.; Fuss-Kailuweit, P.; Dimroth, F.; Witzigmann, B.; Xu, H. Q.; Samuelson, L.; Deppert, K.; Borgström, M. T., InP Nanowire Array Solar Cells Achieving 13.8% Efficiency by Exceeding the Ray Optics Limit. *Science* **2013,** *339* (6123), 1057.
49. Dick van Dam, N. J. J. v. H., Yingchao Cui, Peter J. van Veldhoven, Erik P. A. M. Bakkers, Jaime Gómez Rivas, and Jos E. M. Haverkort, High-Efficiency Nanowire Solar Cells with Omnidirectionally Enhanced Absorption Due to Self-Aligned Indium–Tin–Oxide Mie Scatterers. *ACS Nano* **2016,** *10* (12), 11414-11419.
50. Suckow, S.; Pletzer, T. M.; Kurz, H., Fast and reliable calculation of the two-diode model without simplifications. *Prog. Photovoltaics.* **2014,** *22* (4), 494-501.
51. Hurkx, G. A. M.; Klaassen, D. B. M.; Knuvers, M. P. G., A new recombination model for device simulation including tunneling. *{IEEE} Trans. Electron Devices* **1992,** *39* (2), 331-338.
52. Vincent, G.; Chantre, A.; Bois, D., Electric field effect on the thermal emission of traps in semiconductor junctions. *J. Appl. Phys.* **1979,** *50* (8), 5484-5487.
53. Schenk, A., A model for the field and temperature dependence of Shockley-Read-Hall lifetimes in silicon. *Solid-State Electron.* **1992,** *35* (11), 1585-1596.
54. Breitenstein, O.; Altermatt, P.; Ramspeck, K.; Green, M. A.; Zhao, J.; Schenk, A. In *Interpretation of the Commonly Observed I-V Characteristics of C-SI Cells Having Ideality Factor Larger Than Two*, 2006 IEEE 4th World Conference on Photovoltaic Energy Conference, 7-12 May 2006; 2006; pp 879-884.
55. McIntosh, K. R. Lumps Humps and Bumps: Three Detrimental Effects in the Current-Voltage Curve of Silicon Solar Cells. PhD Thesis, University of New South Wales, Sydney, Australia, 2001.
56. F. Hernando, R. G., G. Bueno., F. Recart, V. Rodriguez Humps, a Surface Damage Explanation. In *2nd World Conference and Exhibition on Photovoltaic Solar Energy Conversion* Vienna, Austria, 1998; pp 1321-1323.
57. Aberle, A. G.; Zhang, W.; Hoex, B., Advanced loss analysis method for silicon wafer solar cells. *Energy Procedia* **2011,** *8*, 244-249.